Phase segmentation of concrete x-ray tomographic images at meso-scale: Validation with neutron tomography

Olga Stamati, Emmanuel Roubin, Edward Andò, Yann Malecot

Phase segmentation of concrete x-ray tomographic images at meso-scale: validation with neutron tomography

Olga Stamati *[1], Emmanuel Roubin[1], Edward Andò[1], and Yann Malecot[1]

[1]Univ. Grenoble Alpes, CNRS, Grenoble INP†, 3SR, F-38000 Grenoble, France

Abstract: This work makes the link between the experimental technique of x-ray tomography and the reliable representation of the heterogeneities of a cementitious material at the meso-scale (aggregates, mortar matrix and macro-porosity). An image analysis procedure and its validation are presented. Images coming **from** x-rays scans are treated to finally obtain a trinary 3D image, where each phase of the material's meso-structure is separated. The separation of the aggregates from the mortar matrix is the technical challenge, due to the physics of x-ray interaction with matter, addressed on this work. Validation of the proposed method is made by comparing the grain size distribution curves computed from images of the same set of aggregates coming from x-rays and neutron scans. The reliably obtained morphology can be used as a basis for direct physical simulations, as well as data to improve morphological models of any type.

Keywords: x-ray tomography, neutron tomography, cementitious materials, concrete, aggregates, porosity, morphological description, image analysis tools, phase segmentation

1. Introduction

At centimeter (meso-) scale, concrete can be considered as a three-phase geomaterial constituted of aggregates and macro-pores (entrapped air porosity) embedded within a mortar matrix. The mechanical behaviour of concrete is the result of the mechanical and morphological properties of these three components and their interfaces ([Basheer *et al.*, 2005], [Zingg *et al.*, 2016], [Piotrowska *et al.*, 2014]). At the meso-scale, aggregates and macro-pores define a key scale of interest for percolating cracks **that greatly increase permeability (and therefore degradation), as well as macro-failure.** Therefore, in recent years, numerical models that explicitly represent the meso-scale have been developed.

One important part of these models is the morphological description of the phases. The most common approach is the use of morphological models (for example, packing of ideal geometrical objects such as spheres ([Lilliu et van Mier, 2003], [Wriggers et Moftah, 2006], [Dupray *et al.*, 2009], [Yin *et al.*, 2012]) or excursions of correlated Random Fields [Roubin *et al.*, 2015]) to generate morphologies that can then be used for multi-physics simulation. These approaches currently face problems regarding the representativeness of the generated morphology, which has dire consequences on the physical response of the model. Often, a volume fraction can be targeted, but global descriptors such as surface areas, mean curvature or topology can be very far from realistic. For this reason, this paper proposes a method for obtaining meso-morphologies from real specimens of concrete, providing a basis for direct physical simulations, as well as data to improve morphological models of any type (with a measurement of real global descriptors, for example).

*e-mail: olga.stamati@3sr-grenoble.fr

†Institute of Engineering Univ. Grenoble Alpes

Real meso-morphologies are obtained by taking advantage of recent advances in non-destructive 3D imaging (in this case x-ray and neutron tomography [Ren *et al.*, 2015], [Van Tittelboom *et al.*, 2013], [Poinard *et al.*, 2012], [Poinard *et al.*, 2011], [Hashemi *et al.*, 2014], [Wildenschild et Sheppard, 2012], combined with image analysis. Isolating phases from an x-ray image is challenging when phases have similar x-ray attenuation coefficients. This unfortunately happens to be the case of concrete's meso-structure (aggregates embedded into mortar matrix) adding considerable difficulty in the identification procedure. Some authors use a series of manual operations (see for example [Yang *et al.*, 2017]), which are extremely time-consuming and certainly not reproducible. The technical challenge of rendering this operation more objective is the principal issue addressed in this work.

This paper, therefore, presents an image analysis procedure to obtain the morphology from x-ray tomography images of concrete. **The segmentation of matrix and aggregates, that have very close mean grey levels, is based on a region-based segmentation technique, that uses the information of the local variance, as has already been used in the medical field [Scholkmann *et al.*, 2010], [Zhan *et al.*, 2013], [Li *et al.*, 2011]. This automatic extraction of aggregates is validated both from scans of aggregates before casting, as well as neutron tomography images.** The resulted morphology can be later used to improve morphological models of any type or as a basis for direct physical simulations. The presented tools are developed independently from any image analysis software, based on simple reproducible functions to encourage further developments, while an open-source release is planned.

2. Problem description

X-ray tomography is a method of reconstructing a 3D field of x-ray attenuation coefficients within an object by assembling 2D radiographic images (projections) taken at different angles. These attenuation coefficients vary according to the atomic number (closely related to density) of the individual materials that compose the investigated object. It is exactly this variation (in attenuation) that makes x-rays so suitable for studying the internal structure of multiphase heterogeneous materials, such as concrete in meso-scale.

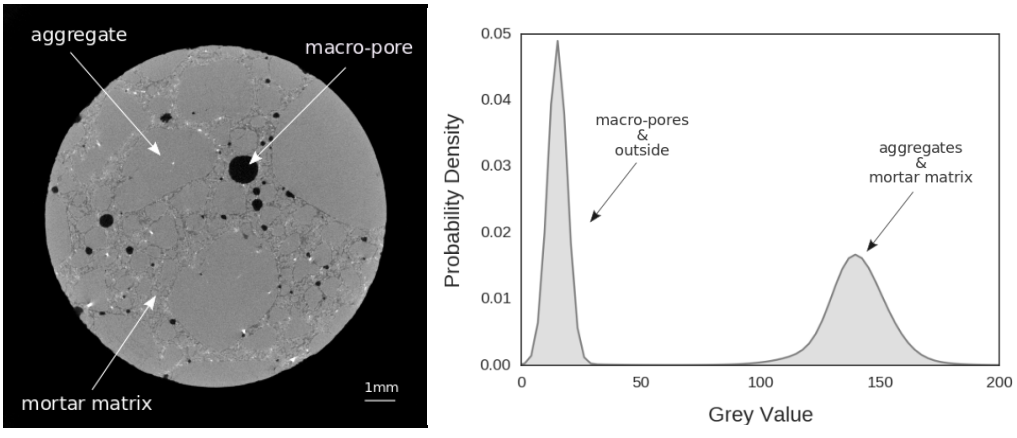

(a) (b)

Figure 1: (a): Characteristic horizontal slice of a reconstructed 3D image coming from a micro-concrete sample x-ray scan, (b): The histogram of its grey values (where the y axis is normalized frequency so that $\int = 1$)

A tomographic scan of a micro-concrete specimen is performed in the x-ray scanner in Laboratoire 3SR (in Université Grenoble Alpes). **The aggregates used are rolled and silicious (chemical composition:** $SiO_2 > 97.3\%$**) coming from Mios (France), with a maximum**

size of 4 mm. The specimen is a cylinder of 11 mm diameter and 23 mm height, selected to capture efficiently the material's meso-structure. The voxel size coming from the scan is 13 μm. The voltage and current of the x-ray source are set to 125 kV and 80 μA, respectively, and the generated x-ray beam is polychromatic of a conical shape. Projections are acquired in 1120 different angular positions between 0°and 360°, as the specimen is rotated around a vertical axis and six images of each angle are averaged in order to reduce the noise.

In Figure 1a, a representative horizontal slice of the reconstructed 3D image is shown. Since it represents a reconstructed field of x-ray attenuation coefficients, where the grey level is high, the area is dense. Consequently, macro-pores appear black, while coarse aggregates and mortar matrix (mix of finer aggregates and sand) share shades of grey. Note that the porosity observed on this scale refers only to the entrapped air porosity formed during the mixing of concrete (macro-porosity). This image contains a certain amount of random noise, which is typically modelled as gaussian, as well as a number of well-known artefacts such *beam hardening* (due to the polychromatic source) and rings.

Although the three phases are easily distinguishable by eye, the 3D image is not easy to trinarise, since the contrast between aggregates and the mortar matrix is well below the noise, resulting in a combined peak in the histogram of Figure 1b. As explained in details in the following section, some post-reconstruction image analysis operations are essential for reducing the noise level and correcting the artificially nonuniform spatial distribution of grey values due to beam hardening. Even assuming no noise or artefacts, considering the fact that the 3D image is composed of discrete voxels of 13 μm size, a range of grey values will still exist, since an intermediate value of two phases is unavoidably measured in their interfaces (known as partial volume effect). Last but not least, from a physical point of view, aggregates and mortar matrix are actually a set of individual particles, albeit of significantly different sizes. When captured at 13 μm size, these different sizes will result in different characteristic distributions of grey values around each material's mean, which will end up to be the key characteristic of their separation.

The separation between the solid and void phases can be achieved with relative ease, due to their obvious density contrast, directly visible on the reconstructed 3D image (see Figure 1). The next section will focus on the proposed procedure of separating the aggregates from mortar matrix by taking into account the *homogeneity* of the x-ray attenuation distribution inside these materials. From an image analysis point of view, this difference (in *homogeneity*) can be revealed by a spatial variance filter.

3. Segmentation procedure

As a first step of the segmentation procedure, a series of post-reconstruction steps are necessary to get the best possible quality of the reconstructed 3D image. First of all, beam hardening is corrected. The unequal repartition of the grey values in the cylindrical specimen studied – with an artificially darkening of the inside – is corrected radially before proceeding into a phase segmentation.

An algorithm is implemented, by collecting grey values of a representative number of randomly distributed macro-pores (lowest grey values) and aggregates (highest grey values) and fitting them, separately for each material, with respect to their radial position (see Figure 2a). Each voxels grey value is then corrected as a function of the specimens radius, **based on the following equation:** $GV^{new}(r) = \frac{GV(r)-GV^p(r)}{GV^a(r)-GV^p(r)}$**, where** $GV^{new}(r)$ **is the corrected grey value for each voxel,** r **is the distance (in pixels) of every voxel to the centre of the specimen,** $GV(r)$ **is the initial grey value of each voxel,** $GV^a(r)$ **and** $GV^p(r)$ **are the fitted initial grey values of the macro-pores and aggregates at a distance** r**, respectively.**

As a further step, for decreasing the noise level, an anisotropic diffusion filter is applied [Perona et Malik, 1990]. A low value (three) is set for the constant conductance parameter in

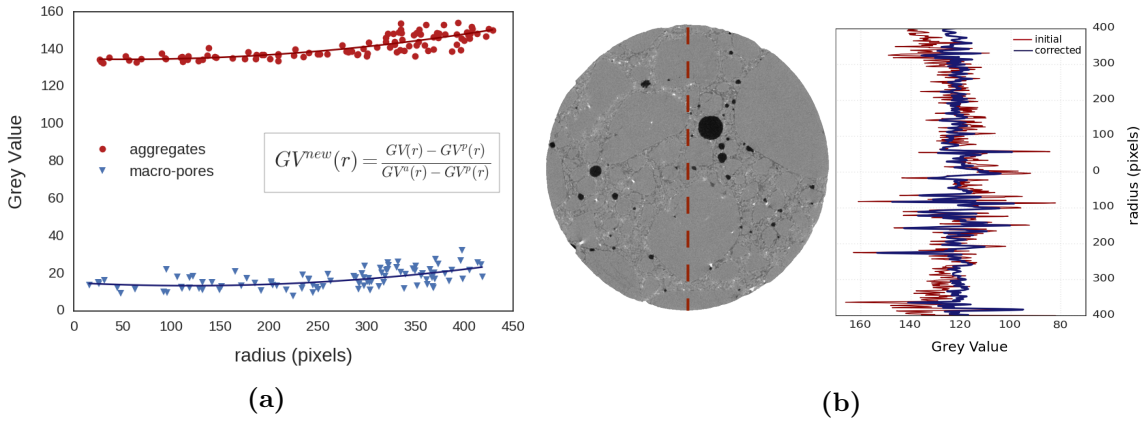

(a) **(b)**

Figure 2: Quality improving operations: (a): *Beam hardening* artefact correction by a new repartition of the grey values (b): Horizontal slice after correcting the *beam hardening* artefact and application of denoising filter, presented with a vertical profile of grey values (crossing the center of the slice) before and after the corrections.

the basic anisotropic diffusion equation, in order to preserve better the image features, mainly the edges of the objects. In Figure 2b, the corrected slice is depicted together with the vertical profiles of grey values crossing the specimen's center before and after the quality improving operations. The artificially lower grey values in the center due to beam hardening are corrected and the high frequency content (random noise) is reduced.

After having improved the quality of the image, the macro-pores segmentation follows (see Figure 3a). As shown in the histogram of Figure 1b, a peak on the left represents the void phase and the outside of the specimen, having lower x-ray attenuation. Macro-pores are defined by implementing an algorithm for thresholding the corrected image, while directly marking and excluding the outside of the specimen from the operation. **In the presented case, the threshold is arbitrarily selected as the minimum between the two peaks in the corrected histogram (see Figure 3b). In cases where the volume fraction of air in the fresh concrete has been measured with an aerometer[1], the chosen threshold value should lead to a macro-pore volume fraction close to the latter, if the imaging resolution is good enough (voxel size $<<$ 50 μm).**

Concerning the separation of coarse aggregates from the mortar matrix, the key lies in another distinguishing characteristic between these two materials, as already introduced in the previous section. Since mortar matrix is by nature a more heterogeneous material compared to aggregates, the *variation* of grey values inside this material should be more irregular. Thus, instead of separating the solid phase based on the *absolute* grey values (density of the material), a separation based on the *variation* of the grey values (homogeneity of the material) is the approach followed and proposed in this work. This is achieved by applying a sequence of morphological operations and filters using structuring elements[2], as explained in details below.

An algorithm for calculating the variance map of a 3D image based on a structuring element, which size and shape can vary according to each specific case is developed. The variance can be given by the formula: $\mathrm{VAR[X]} = \mathrm{E[X^2]} - \mathrm{E[X]^2}$**, where** $E[X]$ **is the averaged grey scale image over the structuring element.** As a general rule, depending on the quality and the spatial resolution of the scan, the structuring element size should be just large enough to separate

[1] Aerometers measure the volume fraction of air in the fresh concrete which after hardening will become porosity due to entrained air (during mixing) and entrapped air (during pouring). The size of this porosity ranges from about 50 μm to about the size of largest aggregates.

[2] A structuring element is a binary matrix that selects a local neighborhood around a voxel of interest and is defined by its shape and its size [Efford, 2000]. As *size* we define the length of the edge of the cube that contains the structuring element (for example, for a cubical structuring element the total number of voxels is $size^3$)

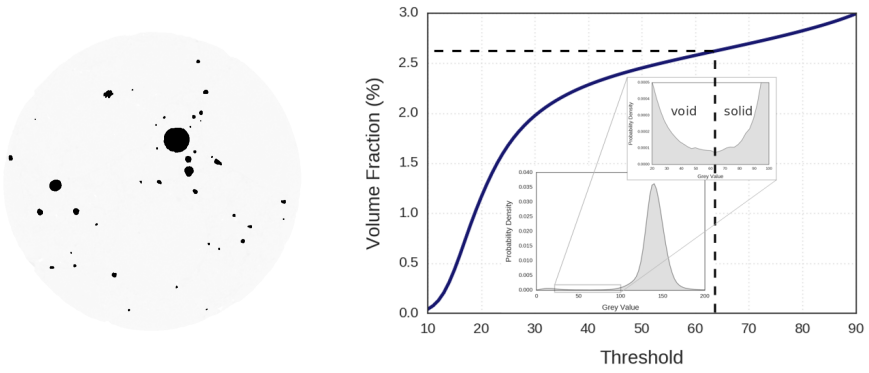

(a) (b)

Figure 3: Segmentation of macro-pores based on a thresholding operation, (a): Binary slice of the macro-pores, (b): Relation between the selected threshold and the resulted macro-porosity. The optimal threshold value is chosen to be the minimum value between the two peaks of the histogram.

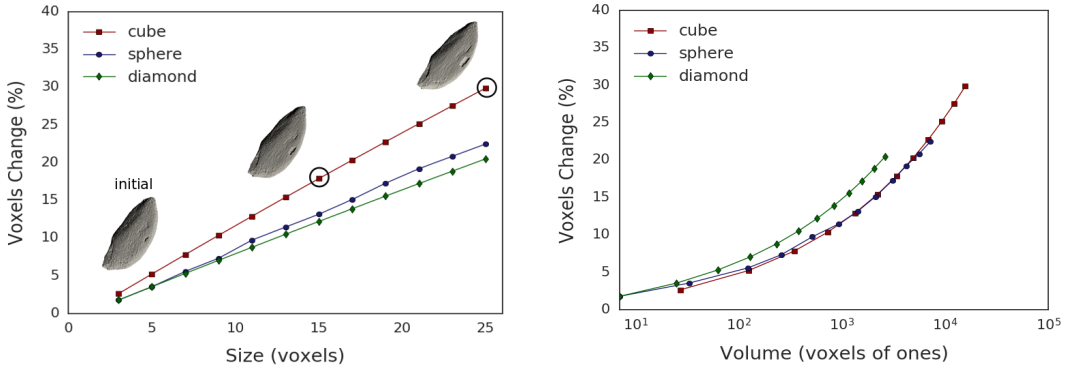

(a) (b)

Figure 4: Deterioration of the aggregates shape during the segmentation process after the application of the variance filter versus (a): the size (length of the edge of the cube that contains the structuring element) of the structuring element. Illustrative example of an aggregate's morphological evolution between the initial state and after the application of a variance filter with a cubical structuring element of 15 and 25 voxels size and (b): the volume (number of ones containing in the binary matrix) of the structuring element.

low and high variance areas, while remaining sufficiently small to detect the smallest aggregates to be segmented. Moreover, structuring element sizes should be minimised to preserve details of the aggregate's shapes.

To evaluate this shape deterioration, the segmentation procedure was applied to already segmented images for several sizes and shapes of structuring elements. The percentage of voxels affected by a change of material during the process was then evaluated. Figure 4a shows the evolution of this percentage versus the size of the structuring element for several structuring element shapes (cube, sphere, diamond) of the variance filter. **An illustrative example of an aggregate's morphological evolution between the initial state (no filter) and after the application of a variance filter with a cubic structuring element of 15 and 25 voxels size is also shown. Concerning the optimal choice of the structuring element, the parameter that most affects the final result is the volume of the structuring element (number of ones contained in the binary matrix), as shown in Figure 4b, while the shape is a second order parameter. However, in our opinion, a spherical structuring element should be generally preferred, since it does not have any preference in orientation and should preserve the details of aggregates shape slightly better, as**

illustrated in Figure 4.

An estimation of the lower limit of the structuring element can be made by assuming that grey levels inside aggregates follow a normal distribution $\mathcal{N}(\mu, \sigma^2)$ with mean μ, and standard deviation σ. After the application of an average filter with the selected structuring element, the standard deviation of the aggregates grey values will be reduced monotonically with the size of the structuring element. A first approximation of the minimal value of the structuring element size can then be given by setting the ratio σ'/μ lower than 3%**, where σ' is the new value of the standard deviation of the grey levels inside the aggregates after the application of the average filter.**

In the presented example (see Figure 5a), a spherical structuring element of 9 voxels size is selected and the variance map of the image is calculated. Considering that the spatial resolution in the 3D reconstructed image is 13 μm/voxel, the smallest object that can be captured is 0.1 mm. Note that the smallest aggregate size used during the casting of the examined micro-concrete specimen was 0.5 mm. Here, it should be mentioned that in lower quality scans (in terms of noise levels) with lower spatial resolutions (around 50 μm/voxel), presented in the following section, a cubical structuring element of 25 voxels has been selected, meaning that aggregates smaller than 1.3 mm can not be captured.

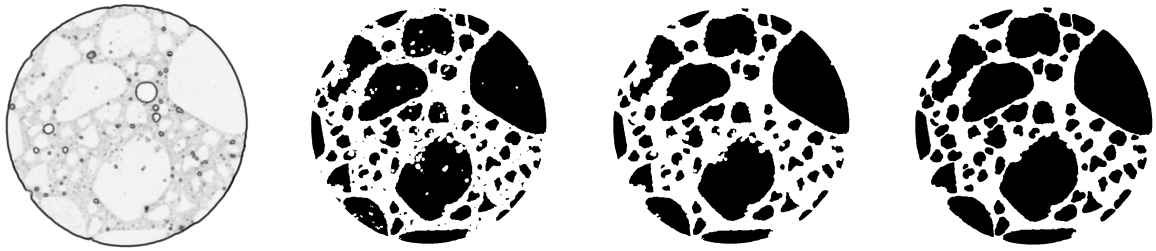

(a) **(b)** **(c)** **(d)**

Figure 5: Developed procedure for extracting the aggregates from a 3D image coming from a concrete x-ray scan. (a): Calculation of the variance map based on a specific structuring element, (b): Thresholding the variance image and keeping only the aggregates, (c): Filling holes and discarding the small size objects and (d): Morphological dilation to retrieve the original size and shape of the objects.

By keeping the lower variance areas (aggregates and macro-pores) and discarding the already segmented macro-pores, a binary 3D image containing the aggregates is obtained (see Figure 5b). A sequence of morphological filters based on structuring elements is then applied on the aggregate binary image so as their original size and shape to be retrieved. An opening morphological operation (for removing the morphological noise) and a filling holes operation (for closing the artificially created holes inside the aggregates) are applied, followed by a sieving operation (for discarding small size objects). In the presented example, based on the aggregate size distribution used for the casting of the micro-concrete sample, any extracted object smaller than 0.5mm is considered part of the mortar matrix and thus discarded. The result of these filters are shown Figure 5c. As a last step, a morphological dilation is applied, so as the original size of the aggregates to be retrieved, using a structuring element of the same shape and half the size of the one selected for the variance filter (see Figure 5d).

By combining the two 3D binary images (one for macro-pores and one for aggregates) the final trinary 3D image is obtained, where each phase is represented strictly by a unique value, as shown in Figure 6. A quantitative analysis for each phase is now possible, by calculating, for example, the aggregate and macro-pore size distribution curves (see Figure 7a). By combining the trinary image with the initial one, the distribution of grey levels inside the aggregates and the mortar matrix are obtained individually for each material (see Figure 7b). The mean values of the two phases are very close: 137 and 134, while the difference in variance is obvious: 5.24

and 15.4, for aggregates and mortar matrix, respectively. Note that after an application of an average filter with the selected structuring element, the standard deviation inside the aggregates is reduced to $\sigma' = 3.3$, leading to a ratio σ'/μ=2.5%. From the probability density functions of Figure 7b, it is obvious that a separation based on a single (mean threshold) value would have been impossible. On the contrary, the difference in variation is rather clear, revealing that the proposed segmentation procedure, based on a variance filter, is a simple, efficient and quite a suitable tool. The segmentation steps presented in this section are highlighted and summarised in a flowchart shown in the Appendix (see Figure A.1).

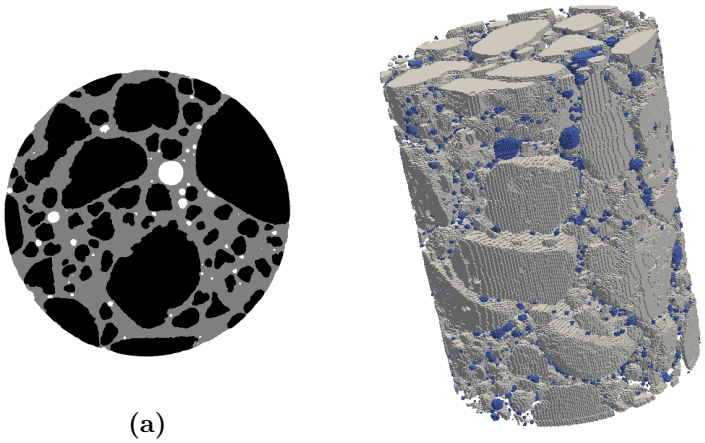

(a) **(b)**

Figure 6: Result of the proposed segmentation procedure: (a): representative horizontal slice as a trinary image where each phase is strictly composed of a set of pixels sharing a unique pre-decided value, (b): the obtained 3D trinary image of the scanned concrete sample, blue: macro-pores, light grey: aggregates and the rest of the volume is occupied by the mortar matrix.

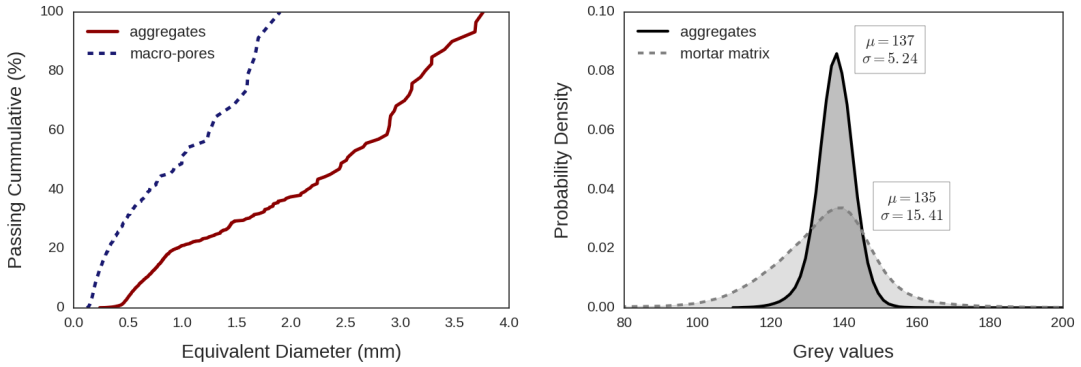

(a) **(b)**

Figure 7: (a): Aggregate and macro-pore size distribution curves, (b): Distribution of grey values inside the aggregates and mortar matrix in the original grey scale image. The resulting mean value and standard deviation are respectively equal to 137 and 5.24 for aggregates, while 135 and 15.41 for mortar matrix.

4. Validation

For the reliability of the segmentation procedure presented in the previous section, a representative set of aggregates, used for an ordinary concrete mix (largest aggregate size of about $1cm$), is embedded into a gel (to limit contacts between aggregates) and scanned with x-rays (see Figure

8a). The aim of this scan is to obtain a binary 3D image of the aggregates surrounded by a low density medium, making them easy to identify, without the need to perform any image analysis operations that may have affected any of their morphological characteristics. Indeed, this time, due to the obvious density contrast between gel and aggregates, the set of aggregates in the reconstructed 3D image is directly extracted through a simple thresholding operation.

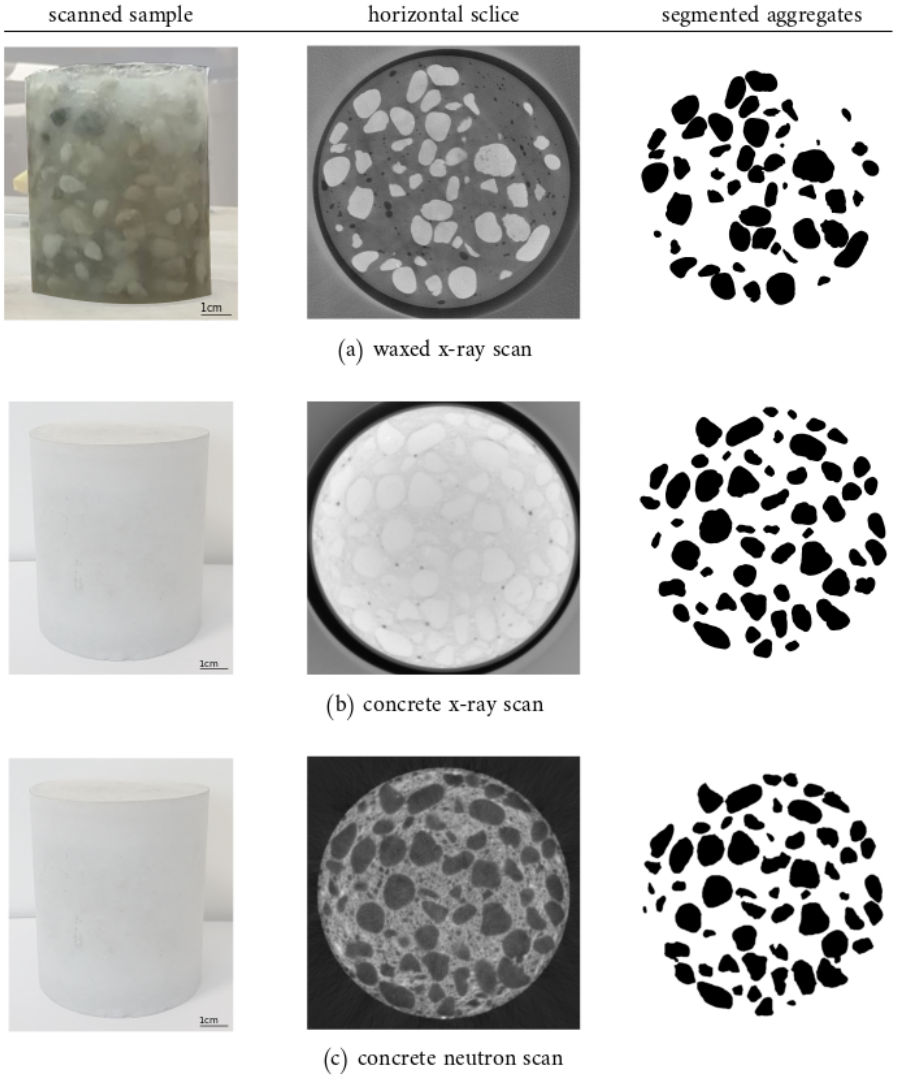

Figure 8: Validation of the aggregates segmentation procedure. A representative set of coarse aggregates is scanned three times and extracted as 3D binary images. (a): embedded in gel, (b): casted as regular concrete and scanned with x-rays, (c): same concrete sample scanned with neutrons.

A mixture and casting of a *real concrete* sample followed, using the exact same set of aggregates, and a new x-ray scan is performed, obtaining a spatial resolution of $50\mu m$/voxel. The procedure presented in the previous section is applied, using a cubical structuring element of 25 voxels size and a second binary 3D image representing the same set of aggregates is obtained (see Figure 8b).

As a further validation step, a neutron tomography scan is performed on the same concrete sample. In this case, due to the physics of neutron interaction with matter, in the reconstructed 3D image, aggregates and mortar matrix do not share the same range of grey values (see Figure 8c). Thus, by applying a thresholding operation based on the absolute (mean) grey values, a third binary 3D image representing the same set of aggregates is obtained, this time coming from a neutron scan.

In the obtained binary 3D images of the extracted aggregates, each individual particle is identified and the three extracted sets of aggregates are compared by plotting the particle size distribution curves (see Figure 9). Note that, concerning the x-ray concrete scan, due to the size of the selected structuring element for the variance filter (cube of 25 voxels size), only aggregates bigger than 1.3 mm are captured. The comparison of the three curves coming from three different scans is satisfactory, **but not enough to prove that the extraction from the concrete x-ray scan is necessarily successful.**

Since the same concrete sample has been imaged by two different modalities (x-rays and neutrons), segmented images can be locally compared. As an illustration, the same horizontal 2D slice as captured firstly from the x-ray and later from the neutron scan is presented on Figure 8b and 8c, respectively. To give a more quantitative evidence, the two 3D binary images of segmented aggregates are registered and then subtracted from one another. The difference of the characteristic 2D slices of Figure 8b and 8c is represented in Figure 10, which shows a good agreement in shape and sizes of the extracted aggregates. The number of voxels that do not coincide between the two segmented 3D images is equal to 4% of the total volume. Assuming that the segmented image obtained from neutron tomography is the reference, this value gives a quantitative order of magnitude of the error of the x-rays scan segmentation procedure. Note that this error would probably be even lower with the images of the micro-concrete sample, presented in Sections 2 and 3, for which unfortunately no neutron scan was performed. According to this validation, the developed and presented procedure leads to a reliable separation of the three phases and consequently to a useful characterisation of concrete's meso-structure, which was the objective of this work.

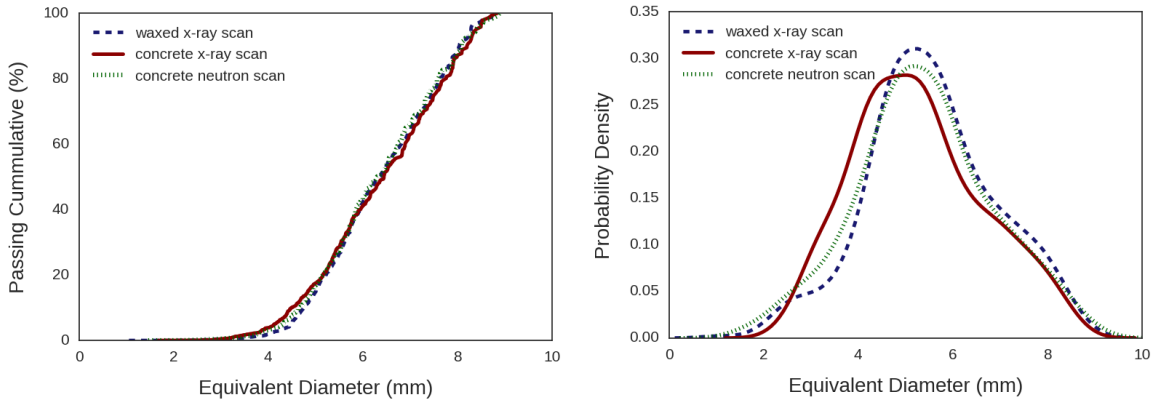

(a) **(b)**

Figure 9: Comparison of the aggregate size distributions coming from the 3 different scans. (a): cumulative distribution function (b): density function (where the y axis is normalized frequency so that $\int = 1$).

5. Conclusion

This work has shown how a 3D grey scale image coming from a concrete x-ray scan can be treated to finally obtain a trinary 3D image, where each phase of concrete's meso-structure is reliably separated. The principal technical challenge of separating the solid phase into aggregates and mortar matrix was successfully achieved, having as a key the segmentation based on the *variation* of grey values inside each material (homogeneity of the material), instead of the *absolute* grey values (density of the material). From an image analysis point of view, the variance map of the grey scale image needed to be computed, according to a selected structuring element. The size

Figure 10: Characteristic slice of the difference between the two binarised 3D images (neutron and x-ray scan).

and the shape of the later can vary according to each case, depending strongly on the noise level and the spatial resolution of the image, setting as a maximum size limit, the minimum aggregate size wanted to be extracted. The distribution of grey levels, in the original grey scale image, individually computed for each phase (after their segmentation), revealed that a segmentation based on a single mean (threshold) value was rather impossible, whereas the implementation of a variance filter was a simple, efficient and very suitable tool for coarse aggregates segmentation.

The proposed procedure has been successfully validated by extracting and comparing the particle size distributions of the same set of aggregates coming from three different scans: aggregates embedded into gel, casting a concrete sample using the exact same set of aggregates and scanned firstly with x-rays and later with neutrons. As a general remark, the proposed procedure has been based on simple reproducible functions and an open-source release is planned. The reliably obtained representation of concrete's meso-scale morphology can provide a basis for direct physical simulations, as well as data to improve morphological models.

6. Acknowledgements

The authors would like to thank Dr. Alessandro Tengattini for performing the neutron scan on the NeXT instrument on D50 at the Institut Laue-Langevin (ILL) in Grenoble.

References

[Basheer *et al.*, 2005] Basheer, L., Basheer, P. et Long, A. (2005). Influence of coarse aggregate on the permeation, durability and the microstructure characteristics of ordinary portland cement concrete. *Construction and Building Materials*, 19(9):682–690.

[Dupray *et al.*, 2009] Dupray, F., Malecot, Y., Daudeville, L. et Buzaud, E. (2009). A mesoscopic model for the behaviour of concrete under high confinement. *International Journal for Numerical and Analytical Methods in Geomechanics*, 33(11):1407–1423.

[Efford, 2000] Efford, N. (2000). *Digital image processing: a practical introduction using java (with CD-ROM)*. Addison-Wesley Longman Publishing Co., Inc.

[Hashemi *et al.*, 2014] Hashemi, M. A., Khaddour, G., François, B., Massart, T. J. et Salager, S. (2014). A tomographic imagery segmentation methodology for three-phase geomaterials based on simultaneous region growing. *Acta Geotechnica*, 9(5):831–846.

[Li *et al.*, 2011] Li, C., Huang, R., Ding, Z., Gatenby, J. C., Metaxas, D. N. et Gore, J. C. (2011). A level set method for image segmentation in the presence of intensity inhomogeneities with application to mri. *IEEE Transactions on Image Processing*, 20(7):2007–2016.

[Lilliu et van Mier, 2003] Lilliu, G. et van Mier, J. G. (2003). 3d lattice type fracture model for concrete. *Engineering Fracture Mechanics*, 70(7):927–941.

[Perona et Malik, 1990] Perona, P. et Malik, J. (1990). Scale-space and edge detection using anisotropic diffusion. *IEEE Transactions on pattern analysis and machine intelligence*, 12(7): 629–639.

[Piotrowska *et al.*, 2014] Piotrowska, E., Malecot, Y. et Ke, Y. (2014). Experimental investigation of the effect of coarse aggregate shape and composition on concrete triaxial behavior. *Mechanics of Materials*, 79:45–57.

[Poinard *et al.*, 2012] Poinard, C., Piotrowska, E., Malecot, Y., Daudeville, L. et Landis, E. N. (2012). Compression triaxial behavior of concrete: the role of the mesostructure by analysis of x-ray tomographic images. *European Journal of Environmental and Civil Engineering*, 16(sup1):s115–s136.

[Poinard *et al.*, 2011] Poinard, C., Piotrowska, E., Marin, P., Malecot, Y. et Daudeville, L. (2011). Mesoscopic scale modeling of concrete under triaxial loading using x-ray tomographic images. *2nd International Conference on Particle-Based Methods - Fundamentals and Applications (Particles) Location: Barcelona, SPAIN Date: OCT 26-28, 2011 Sponsor(s):Tech Unive Catalonia; Swansea Univ; European Community Computat Methods Appl Sci (ECCOMAS); Int Assoc Computat Mech (IACM)*, pages 117–129.

[Ren *et al.*, 2015] Ren, W., Yang, Z., Sharma, R., Zhang, C. et Withers, P. J. (2015). Two-dimensional x-ray ct image based meso-scale fracture modelling of concrete. *Engineering Fracture Mechanics*, 133:24–39.

[Roubin *et al.*, 2015] Roubin, E., Colliat, J.-B. et Benkemoun, N. (2015). Meso-scale modeling of concrete: A morphological description based on excursion sets of Random Fields. *Computational Materials Science*.

[Scholkmann *et al.*, 2010] Scholkmann, F., Spichtig, S., Muehlemann, T. et Wolf, M. (2010). How to detect and reduce movement artifacts in near-infrared imaging using moving standard deviation and spline interpolation. *Physiological measurement*, 31(5):649.

[Van Tittelboom *et al.*, 2013] Van Tittelboom, K., Snoeck, D., Vontobel, P., Wittmann, F. H. et De Belie, N. (2013). Use of neutron radiography and tomography to visualize the autonomous crack sealing efficiency in cementitious materials. *Materials and structures*, 46(1-2):105–121.

[Wildenschild et Sheppard, 2012] Wildenschild, D. et Sheppard, A. P. (2012). X-ray imaging and analysis techniques for quantifying pore-scale structure and processes in subsurface porous medium systems. *Advances in Water Resources*, 51(January 2013):217–246.

[Wriggers et Moftah, 2006] Wriggers, P. et Moftah, S. (2006). Mesoscale models for concrete: Homogenisation and damage behaviour. *Finite elements in analysis and design*, 42(7):623–636.

[Yang *et al.*, 2017] Yang, Z., Ren, W., Sharma, R., McDonald, S., Mostafavi, M., Vertyagina, Y. et Marrow, T. (2017). In-situ x-ray computed tomography characterisation of 3d fracture evolution and image-based numerical homogenisation of concrete. *Cement and Concrete Composites*, 75:74–83.

[Yin *et al.*, 2012] Yin, A., Yang, X., Gao, H. et Zhu, H. (2012). Tensile fracture simulation of random heterogeneous asphalt mixture with cohesive crack model. *Engineering Fracture Mechanics*, 92:40–55.

[Zhan *et al.*, 2013] Zhan, T., Zhang, J., Xiao, L., Chen, Y. et Wei, Z. (2013). An improved variational level set method for mr image segmentation and bias field correction. *Magnetic Resonance Imaging*, 31(3):439–447.

[Zingg *et al.*, 2016] Zingg, L., Briffaut, M., Baroth, J. et Malecot, Y. (2016). Influence of cement matrix porosity on the triaxial behaviour of concrete. *Cement and concrete research*, 80:52–59.

A. Appendix

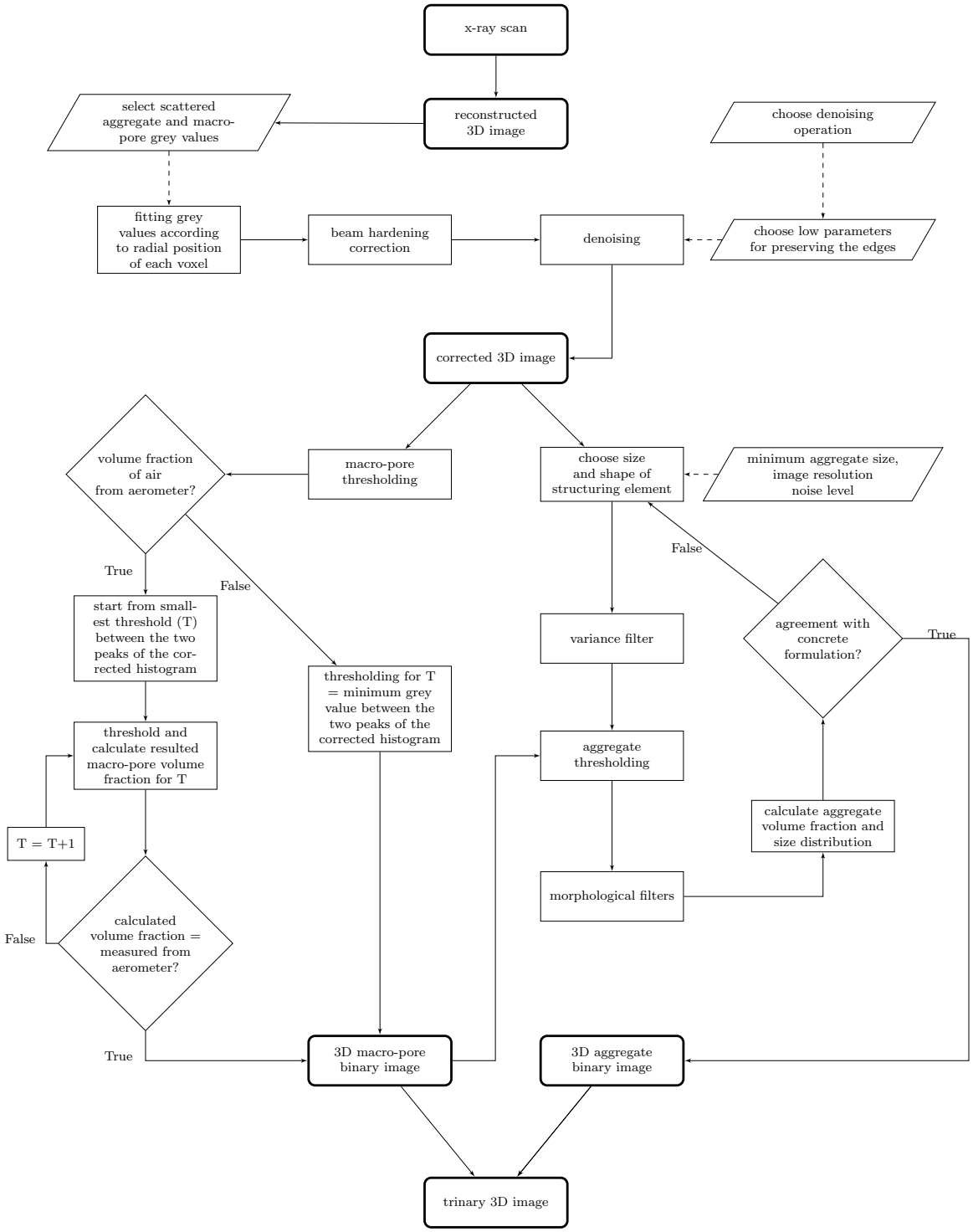

Figure A.1: Flowchart of the proposed segmentation procedure.